Eur. Phys. J. A **17**, 595–605 (2003)
DOI 10.1140/epja/i2002-10164-y

THE EUROPEAN PHYSICAL JOURNAL A

Study of the reaction pp → ppπ^0 within 10 MeV above the threshold

The COSY-TOF Collaboration

S. Abd El-Samad[5], R. Bilger[4], A. Böhm[2], K.-Th. Brinkmann[2], H. Clement[4], S. Dshemuchadse[6], W. Eyrich[3], D. Filges[5], H. Freiesleben[2], M. Fritsch[3], R. Geyer[5], D. Hesselbarth[5], B. Jakob[2], L. Karsch[2], K. Kilian[5], H. Koch[1], J. Kress[4], E. Kuhlmann[2,a], S. Marwinski[5], P. Michel[6], K. Möller[6], H.P. Morsch[5], L. Naumann[6], M. Richter[2], E. Roderburg[5], M. Rogge[5], A. Schamlott[6], M. Schmitz[5], P. Schönmeier[2], W. Schroeder[3], M. Schulte-Wissermann[2], M. Steinke[1], F. Stinzing[3], G.Y. Sun[2], G.J. Wagner[4], M. Wagner[3], A. Wilms[1], and S. Wirth[3]

[1] Institut für Experimentalphysik, Ruhr-Universität Bochum, D-44780 Bochum, Germany
[2] Institut für Kern- und Teilchenphysik, Technische Universität Dresden, D-01062 Dresden, Germany
[3] Physikalisches Institut, Universität Erlangen, D-91058 Erlangen, Germany
[4] Physikalisches Institut, Universität Tübingen, D-72076 Tübingen, Germany
[5] Institut für Kernphysik, Forschungszentrum Jülich, D-52425 Jülich, Germany
[6] Institut für Kern- und Hadronenphysik, Forschungszentrum Rossendorf, D-01314 Dresden, Germany

Received: 4 December 2002 / Revised version: 28 April 2003 /
Published online: 29 July 2003 –
Communicated by M. Garçon

Abstract. Kinematically complete measurements of the $pp \to pp\pi^0$ reaction were performed for beam energies in the range 292–298 MeV. We detected both protons in coincidence by using the large-acceptance COSY-TOF spectrometer and an external proton beam at COSY-Jülich; thus, we measured total and differential cross-sections and energy distributions. A strong enhancement was observed in the Dalitz plots due to the final-state interaction between the two outgoing protons; the data are well reproduced by Monte Carlo simulations using a standard scattering length of $a_0 = -7.83$ fm and effective range of $r_0 = 2.8$ fm. Our measured total cross-sections are roughly 50% larger than those of recent internal-target experiments at IUCF and CELSIUS. This discrepancy may be due to the final-state interaction pushing some events into the very small-angle region which is almost inaccessible to an internal-target experiment. In the angular distributions we found only very slight deviations from isotropy. The analysis of our momentum distributions yielded a small fraction of $5 \pm 5\%$ for Ps or Pp wave contributions.

PACS. 13.75.Cs Nucleon-nucleon interactions (including antinucleons, deuterons, etc.) – 25.10.+s Nuclear reactions involving few-nucleon systems – 25.40.Ep Inelastic proton scattering – 29.20.Dh Storage rings

1 Introduction

The last decade saw a renaissance of near-threshold pion-producing reaction studies in nucleon-nucleon (NN) collisions. With the advent of medium-energy accelerators in Bloomington/USA (IUCF), Uppsala/Sweden (CELSIUS), and Jülich/Germany (COSY) a wealth of high-precision data on total and differential cross-sections as well as polarization observables was measured for the reactions $pp \to pp\pi^0$ [1–6], $pp \to pn\pi^+$ [7–9] and $pp \to d\pi^+$ [10,11], which, in turn, induced a flurry of theoretical activity [12–18]. So far, good agreement is found in the theoretical description of the reactions $pp \to d\pi^+$ and $pp \to pn\pi^+$, larger discrepancies are observed for the $pp \to pp\pi^0$ reaction. Soon after the publication of the near-threshold data on neutral-pion production it was recognized that the $pp\pi^0$ reaction near threshold is sensitive to short-range mechanisms in the NN system. Since the main pion exchange term, which dominates the charged-pion–producing channels, is isospin-forbidden, Lee and Riska proposed to counter this shortfall by the additional consideration of pair diagrams with an exchanged heavy meson (σ, ω) [12]. Likewise the role of pion rescattering only then was treated with more concern, but also in a somewhat controversial manner, since field-theoretical models and chiral perturbation theories found different relative signs in the π exchange amplitude with respect to the direct (Born) term [13,14,17]. Attempts have been pursued to additionally include $\Delta(1232)$-isobar and S_{11} and D_{13} nucleon

[a] e-mail: e.kuhlmann@fz-juelich.de

resonance excitations [15–17]. To date, calculations in the framework of the Jülich meson exchange model [17,18], which incorporate all the basic terms like heavy-meson exchange (HME), delta-resonance and off-shell effects, as well as realistic final-state interactions, yield the best results; with the exception of the strength parameter of the HME term the model needs no adjustable parameters.

Close to threshold only a few partial waves have to be considered with Ss, Sp, Ps and Pp being the leading ones, whereas the role of $l = 2$ contributions (Sd and Ds) is still under debate. Here, the Rosenfeld notation $L_p l_q$ has been used [19] with L_p being the orbital angular momentum of the NN pair, l_q that of the pion with respect to this pair. In the $pp\pi^0$ reaction the partial wave Sp, which, apart from Ss, governs the isoscalar reaction channels $d\pi^+$ and $pn\pi^+$, is forbidden by conservation laws. As a result, purely isotropic angular distributions are found for the $pp\pi^0$ reaction in the region up to 10 MeV above threshold [3]. Also, sizeable analyzing powers are only observed for this reaction for excess energies Q higher than 16 MeV [4], which follows from the fact that interference effects are only possible between amplitudes (Ps, Pp) on the one hand or (Ss, Sd, Ds) on the other. Except for Ss, however, the magnitude of all these amplitudes is negligibly small up to $Q = 16\,\mathrm{MeV}$. For comparison, angular distributions as well as analyzing powers extracted from a study of the π^+-producing reactions show clear evidence for the presence of Sp, and hence $l = 1$ contributions at energies as low as 2 MeV above threshold [10,11].

Measurements very close to threshold, where all escaping particles are confined to a narrow cone around the beam axis, require a perfectly matched detector system which has to cover as much of the available phase space as possible in order to keep necessary acceptance corrections to a minimum. In Jülich, the COSY-TOF spectrometer, a scintillator hodoscope of cylindrical shape with full ϕ-symmetry, fulfills these requirements to a very large extent. Charged particles are detected at polar angles as close as one degree to the beam. In the past we have used this spectrometer in meson and hyperon production studies and pp bremsstrahlung experiments. Parallel to the analysis of the bremsstrahlung reaction [20], data obtained simultaneously for $pp \to pp\pi^0$ were analysed as a cross-check. We systematically found larger cross-sections than given in [1,3]. Since the results we deduced from the data for the concurring charged-π–producing reactions agreed nicely with the published values [7,10,11], whereas the cross-sections for π^0 production remained high, we decided to perform a second experiment to clarify that matter.

In this paper we will present data from a kinematically complete measurement of the reaction $pp \to pp\pi^0$ for three energies in the range 292–298 MeV, corresponding to beam momenta of 796–805 MeV/c. Total cross-sections as well as angular and energy distributions will be shown and compared to Monte Carlo simulations which are based on phase-space–distributed events that are modified by the final-state interaction (FSI). Results of the concurring reactions $pp \to d\pi^+$ and $pp \to pn\pi^+$ which were obtained in parallel will only be given to underline the performance of the spectrometer and to prove the consistency of the analysis. Apart from the excess energy Q we will also use the dimensionless parameter η for labelling energies above threshold defined as $\eta = q_{\max}/m_\pi$ with q being the CM momentum of the pion and m_π its mass. With p we denote the CM momentum of one proton in the two-proton subsystem. The angles Θ_q and Θ_p (in the CM system) are taken with respect to the beam. The momenta q and p are linked by energy conservation via $\sqrt{s} = \sqrt{m_\pi^2 + q^2} + \sqrt{M_{pp}^2 + q^2}$ and $M_{pp}^2 = 4(m_p^2 + p^2)$, where s is the square of the total CM energy and M_{pp} the invariant mass of the two protons.

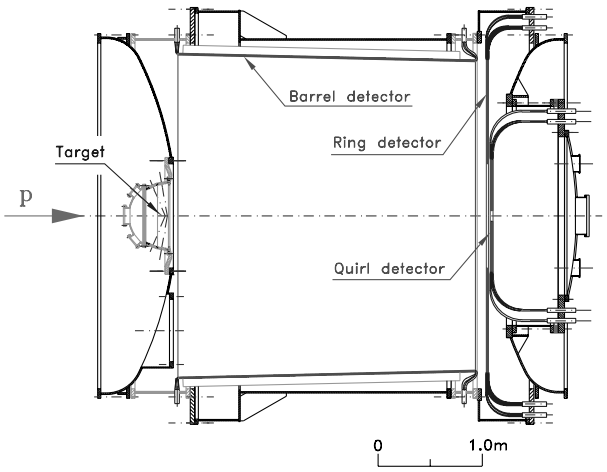

Fig. 1. Sketch of the COSY-TOF spectrometer.

2 Experimental procedure

2.1 Apparatus

The experiment was carried out with the time-of-flight spectrometer COSY-TOF [21,22] set up at an external beam line of the 2.5 GeV proton synchrotron COSY at Jülich/Germany. The goal was to study simultaneously and with the same spectrometer all five reaction channels which are open in pp collisions at beam energies near 300 MeV. Besides pp elastic scattering, which is by far the strongest, and the very weak pp bremsstrahlung, our interest mainly aimed at the π-producing reactions $pp \to d\pi^+$, $pp \to pp\pi^0$, and $pp \to pn\pi^+$, each one with cross-sections rising fast with excess energy.

A schematic sketch of the spectrometer showing the locations of the main components, the barrel (B), ring (R), and quirl (Q) detector, as well as the target region is given in fig. 1. To prevent the reaction products from undergoing secondary reactions on their way from the target to the different detector modules of the spectrometer it is housed within a $3.3\,\mathrm{m}\varnothing \times 4\,\mathrm{m}$ steel tank which can be evacuated to a pressure of 0.2 Pa. Protons were extracted out of the COSY ring in a slow-extraction mode allowing spill lengths of up to 10 min. Their intensity typically was of the order of several 10^6/s. The beam was focussed onto the liquid-hydrogen target with dimensions

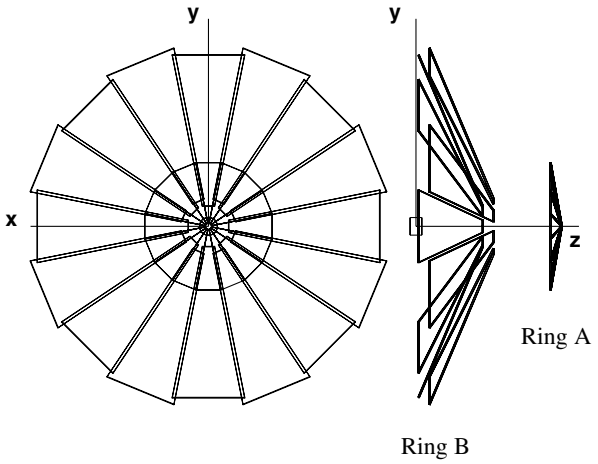

Fig. 2. Front and side view of the start detector. The target is placed to the left of ring B.

6 mm$\varnothing \times 4$ mm [23]. Its front and rear ends were closed by 0.9 μm thin Hostaphan foils. A set of scintillator veto detectors with central holes of various sizes were located 260, 51 and 3.5 cm upstream of the target. They helped to define the beam spot in the center of the target to an area with diameter $d = 3.0$ mm. Charged particles emitted from the target into the forward hemisphere had to transverse a 0.5 mm thin plastic scintillator device [24] which served as start detector. This detector shown in fig. 2 consists of two concentric rings made out of 16 trapezoidally shaped scintillators each, which were placed 30 mm (Ring B) and 50 mm (Ring A) behind the target. The inner detector had a central hole of diameter $d_i = 3.3$ mm and extended out for 26 mm, the outer one had dimensions $d_i = 16$ mm and $d_a = 130$ mm. The minimum angle for observable ejectiles was 1.9°, if they originated from the center of the target, but smaller values far less than 1.0° were possible if the initial pp reaction took place off the beam axis. The elements of the outer ring were arranged in such a way as to show a tiny overlap along their sides thus guaranteeing full ϕ-coverage, whereas the ones of the inner ring were only allowed to touch each other thereby leaving narrow gaps of order 50 μm which caused an overall loss in ϕ-coverage of 3% distributed evenly over the full circle.

After a flight path of up to 3 m in vacuum, the reaction products hit the 3-component (B, R, and Q) scintillator hodoscope. The circular, 3-layer quirl and ring detector components of the endcap were both built according to the same layout. Five mm thin scintillator sheets (BC408) were used as basic material. The first layer in the quirl is made from 48 wedge-like scintillators, followed by two layers with 24 left- and 24 right-wound elements, each element cut along an Archimedian spiral [21]. In central projection a net-like pattern is formed consisting of more than 1000 triangular pixels. A central hole of radius $r = 4.2$ cm was left for the beam, the outer radius of the quirl is 58 cm. The three layers in the ring were made from 96 wedges and 2×48 left- and right-wound Archimedian spirals, the inner (outer) radius is 56.8 (154) cm, respectively. The barrel consists of 96 scintillator bars, mounted to the inside of the tank. Each bar of 2.85 m length has a cross-section with measures thickness $\times$ width = 15 mm $\times$ 96 mm and is read out from both ends [22].

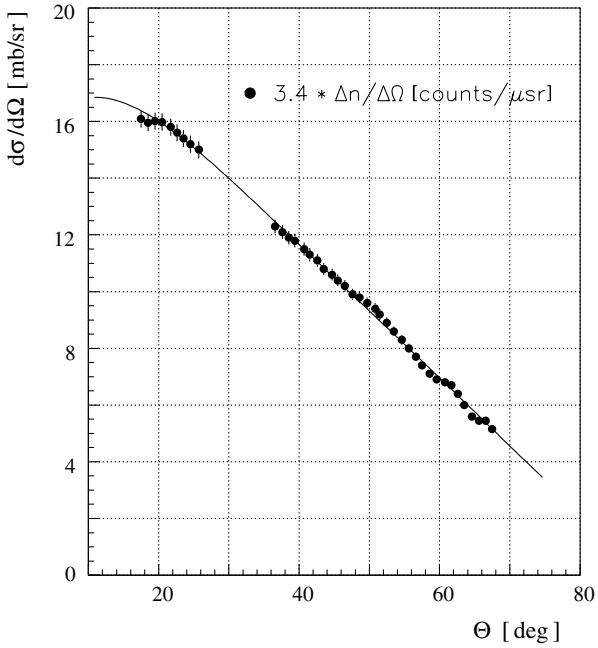

Fig. 3. Measured angular distribution of elastic pp scattering events (solid dots) compared to the SAID solution (full line, see text).

In the course of the experiment which went on for almost two years, two slightly different set-ups were employed. The one described above with barrel, ring and quirl was used at $T = 293.5$ MeV. Azimuthal coverage was complete, the acceptance in polar angle θ ranged from 1.5°–78°. In an earlier experiment performed at $T = 292.2$ and 298.1 MeV the ring component was still under construction, leaving a gap in polar angle θ between 10.4°–26°. For this run a modular neutron detector [25] was additionally set up downstream around the beam line and outside of the tank. It covered approximately the same area as the quirl detector and was employed in the study of the concurring $pp \to pn\pi^+$ reaction. As a first-level trigger usually one, in some cases two charged hits were required in the start detector, at least two in any of the stop detectors B, R, Q, with 2B, 2R, 2Q and 2(BRQ) denoting separately handled trigger patterns. For each of these patterns slightly different dead-times were observed and the necessary corrections had to be applied accordingly.

2.2 Performance checks and luminosity monitor

Simultaneously with the π-producing reactions, elastic-scattering events, which were detected either as barrel-barrel (BB) or as barrel-ring (BR) coincidences, were written on tape. In addition to serving as a tool for calibrating the whole detector system, this reaction was used as a luminosity monitor through comparison of experimentally deduced elastic-scattering events with data taken from the SAID database [26] (see fig. 3). The cross-section around

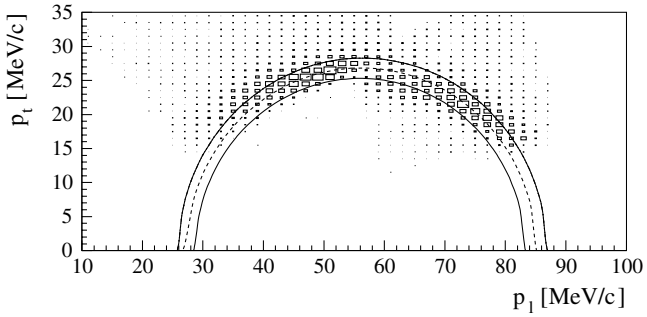

Fig. 4. Transverse *vs.* longitudinal π momentum in comparison with expectations from two-body kinematics for three different beam energies (see text for details).

$T = 300\,\mathrm{MeV}$ is known with an error of less than 5%. Any cross-section of interest determined relative to the one for pp_{elast} will thus be measured with comparable accuracy, since all uncertainties resulting from instabilities in beam intensity and target thickness cancel.

We obtained complementary information on the detector performance from a careful study of the $pp \to d\pi^+$ reaction. Its cross-section at 295 MeV is close to $45\,\mu$b [10]. While the deuterons with a maximum polar angle at 3° will only reach the quirl, the pions with $\theta^{\max} = 32°$ can be observed in all of the three stop detector components. The unique kinematics of this 2-particle reaction allowed the extraction of rather clean and almost background-free spectra as, *e.g.*, invariant d and π^+ mass distributions. In the present case this reaction was used for an accurate determination of the beam energy T_p, which is important in view of the strong T_p dependence of the cross-section as well as available phase space coverage, which in turn has a strong impact on the acceptance correction. In fig. 4 the transverse π momentum p_{t} is plotted *versus* the longitudinal π momentum p_{l}. The boxes represent the experimental data, their sizes being proportional to the respective number of counts. Concentration of yield is observed along an elliptical curve which aligns nicely with the one resulting from two-body kinematics for a beam energy of $T_p = 293.5\,\mathrm{MeV}$ (dashed curve). The two solid lines calculated for beam energies, which are 0.6 MeV higher and lower, clearly miss the main body of the data from which we deduce an error in beam energy of order 0.3 MeV.

The modulation in yield along the elliptical curve and the absence of yield for p_{t} values below 17 MeV/c is well understood and can be explained as stemming from particular technical details in detector construction as well as the rather low pion momenta: pions emitted at angles larger than 26° will be observed in the one-layer barrel section; these are the events with p_{l} up to 52 MeV/c. Those with very low momenta, however, will not be able to reach it. The ring section covers the range 10.4°–26°; here, however, a pion has to reach at least the second layer in order to fix its point of impact, hence a decrease in yield is observed for pion angles approaching the outer range of the ring. Very forward pions with low p_{t} values were not observed, since the coincident deuterons escaped through the central hole in the start detector.

3 Data analysis and calibration

3.1 Principle of measurement

The photomultiplier signals of all detector elements were used for energy loss as well as time-of-flight measurements. To this end, the analog signals were digitized in Fastbus-QDC modules, the timing signals were derived in leading-edge–type discriminators and used in Fastbus TDCs. Both measurements yield the particle velocity β. From the particle's point of impact the flight direction was obtained, from which two additional observables, θ and ϕ, can be derived. In the endcap with its 3-layer quirl and ring components the flight direction is deduced by combinatorial means [21]. For the one-layer barrel elements with two-sided read-out the point of impact is found from the difference in TDC values of both ends [22], whereas the TDC sum is a measure of the flight time. The spatial resolution as given from the pixel size in the endcap is $\Delta\theta = 0.5°, \Delta\phi = 2°$; roughly the same values hold for the barrel elements. Typical values obtained for the time resolution of the start-stop system were of the order of 0.5 ns (FWHM), which corresponds to about 2.5% of the average flight time of a $\beta = 0.5$ particle.

The momentum 4-vector of each detected particle can then be deduced from the measured observables β, θ, and ϕ by applying an additional mass hypothesis. This, of course, has to be checked in comparison with results obtained from Monte Carlo simulations. In case of a reaction with one neutral particle like $pp \to pp\pi^0$, the 4-vector of that particle is deduced by employing energy and momentum conservation and calculating its mass.

3.2 Calibration

In order to determine θ, ϕ and β for each particle, several steps in calibrating the detector had to be performed [27]. After a simple pedestal subtraction in the QDC spectra, a walk correction had to be applied for each TDC entry. Depending on the pulse height of the scintillator signal, time shifts of up to 3 ns were observed. To correct for these shifts a five-parameter fit function was found which relates the observed walk with the pulse height given by the corrected QDC value. The complete parameter list for up to 600 scintillator channels was determined before each experiment. This was routinely done by use of a laser-based calibration system where UV light from a N_2-laser is fed via quartz fibers into each of the individual scintillator channels. Through use of a set of filters the amount of light going into the various elements can be varied such as to cover the complete dynamic range of the multipliers.

A check on the differential nonlinearity in the TDC modules revealed no deviations from the precision given by the manufacturer ($< 0.1\%$ of full scale), in some cases, however, a channel width of 90 ps/channel was observed instead of the preset value of 100 ps/channel. Due to different cable lengths and varying transit times in the photomultiplier tubes and electronic modules, variations in

the signal arrival time arise which are specified as TDC-offsets. These offsets were determined in an iterative manner by first comparing overlapping, but otherwise identical channels as, *e.g.*, neighboring elements in the outer start detector (sect. 2.1) or overlap regions from left- and right-wound elements in the endcap. Two-particle reactions like pp_{elast} and $d\pi^+$ with their unique kinematics then were used for the adjustment of all remaining detector components. As a by-product, the light velocities within the differently shaped scintillator elements were deduced. Whereas in bulk material it is given by c/n (n: index of refraction), smaller values were found for the rather flat, but long elements due to an effective lengthening of the light path. For the straight quirl elements of wedge-like shape and a thickness of 5 mm we found 18.0 cm/ns, for the corresponding ones of the ring 15.8 cm/ns. A value of 16.1 cm/ns was observed for the 3 m barrel elements. The calibration of the neutron detector with its 10 cm thick bars was performed as outlined in [25]. Special care was applied in the determination of the energy-dependent efficiency which, for neutron energies larger than 60 MeV, was found to be rather constant around 13.5%.

3.3 Monte Carlo simulation

Throughout the analysis each step was compared to the results deduced from the Monte Carlo simulation. The program package written in C^{++} was developed in Bochum [28,29] with the purpose of simulating the spectrometer response, thereby giving insight into the overall performance, and to determine the detector acceptance. At its core is the CERNLIB random event generator GENBOD [30], which generates a preset number of N-body events for a given reaction specified by N, the number of ejectiles, their masses and the 4-momentum of the incoming beam. It returns momentum 4-vectors for each particle in the overall center-of-mass system, and weight factors w_{e} based on the phase space density of the reaction. These weight factors have to be modified, if angular momentum or final-state interaction effects are believed to play a substantial role. The Monte Carlo code then boosts this event into the laboratory system and each particle is tracked through the complete set-up. Nuclear interactions are treated according to the INC code [31] which has its roots in the Bertini intranuclear cascade model of the late sixties [32]. This model assumes the nucleons within their respective nuclei to behave like a Fermi gas and the interactions between the incident particle and the nucleus is simulated as the output of an intranuclear particle shower with nucleon-nucleon and pion-nucleon reactions. Elastic and inelastic NN and πN cross-sections are supplied via extensive data tables. Great care was put into modelling all of the detector components in their particular shape as close as possible to reality, including the left- and right-wound spirals in the endcap and the trapezoidal elements of the slightly conical barrel detector. Options were built into the program to study in detail the influence of the extended target and the transverse beam spread or the variation in acceptance due to the narrow gaps between neighboring scintillator elements or the size of the central hole in the inner start detector.

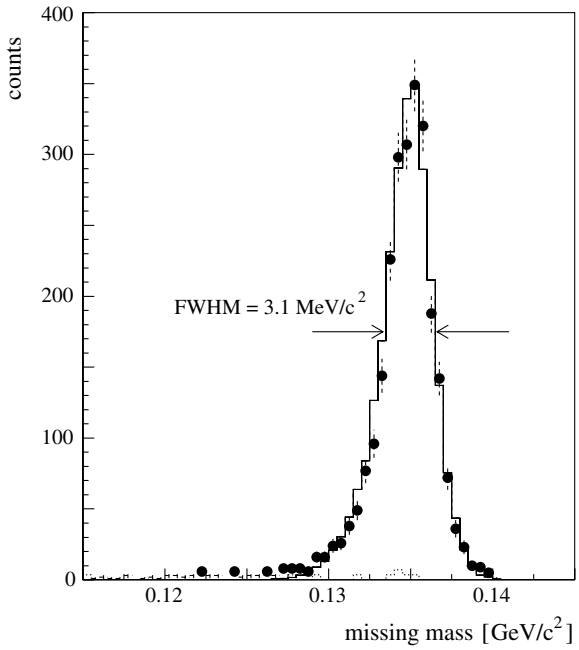

Fig. 5. Missing-mass spectrum of reconstructed $pp\pi^0$ events (dots with error bars) in comparison with the Monte Carlo simulation (histogram). The dashed histogram shows the normalized spectrum obtained with an empty target.

In the course of the simulation, interactions of the particles on their way through the various active or passive detector parts can be switched on or off, their energy loss and small-angle scattering can be investigated separately. Effective low-energy thresholds can thus be studied in detail as, *e.g.*, in case of the endcap, where a hit in at least two layers is needed for a successful pixel reconstruction. Also included in the Monte Carlo package is the possibility of particle decay. In the present case it was found that a sizeable fraction of the π^+-mesons with low momentum had decayed before the detector was reached and a decay muon was detected instead.

4 Results

4.1 Total cross-sections

By use of energy and momentum conservation, the $pp\pi^0$ events were identified by calculating the missing mass m_x of the unobserved neutral pion according to

$$m_x^2 = (\mathbb{P}_{\mathrm{b}} + \mathbb{P}_{\mathrm{t}} - \mathbb{P}_1 - \mathbb{P}_2)^2 \,, \qquad (1)$$

where $\mathbb{P}_{\mathrm{b}}(\mathbb{P}_{\mathrm{t}})$ denotes the beam (target) momentum 4-vector, respectively, and $\mathbb{P}_i$ the one of the i-th proton. The high-energy part of the distribution obtained at $T = 293.5\,\mathrm{MeV}$ is given in fig. 5 showing a clear signal at the expected location $m_x = m_\pi = 0.135$ GeV/c^2.

The only cuts applied in the analysis were upper limits on the β values of the protons in order to eliminate events

Table 1. Total $pp \to pp\pi^0$ cross-sections derived at three beam energies. The column labelled acc lists the detector acceptance as determined from our Monte Carlo simulations based on FSI modulated phase-space–distributed events.

T (MeV)	η	N_π	acc	$\int L\mathrm{d}t\,(\mathrm{nb}^{-1})$	$\sigma_{\mathrm{tot}}\,(\mu\mathrm{b})$
292.2 ± 0.3	0.29	1586	0.55	1.25	2.31 ± 0.06 ± 0.23
293.5 ± 0.3	0.30	2524	0.64	1.41	2.80 ± 0.06 ± 0.21
298.1 ± 0.2	0.35	4426	0.49	2.43	3.72 ± 0.06 ± 0.28

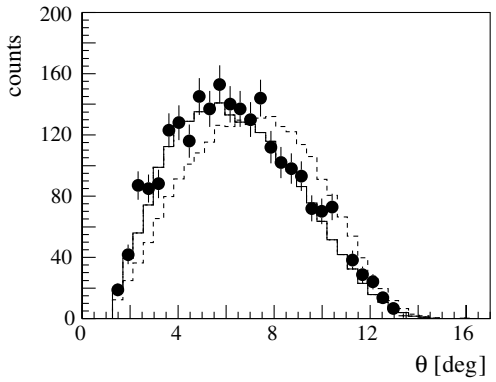

Fig. 6. Proton angular distribution obtained at $T = 293.5\,\mathrm{MeV}$ in the laboratory system. The solid (dashed) histogram shows Monte-Carlo–generated results, where final-state interaction effects have been included (omitted).

where a much faster pion was wrongly interpreted as a proton. Background due to reactions on the target foils or condensates thereon is negligible as can be seen from the spectrum obtained from an empty target run and shown by the dashed histogram in fig. 5. Also displayed is the result of our Monte Carlo simulation (solid histogram) which is in excellent agreement with the data. The angular distribution of the inelastically scattered protons is shown in fig. 6 (solid dots with error bars) together with results of our Monte Carlo simulations. A shift towards smaller proton angles and away from purely phase-space–distributed events (dashed histogram) is readily seen. When incorporating final-state interaction effects into the Monte Carlo code, however, and using standard values for effective range r_0 and scattering length a, the simulated curve nicely reproduces the data as shown by the solid histogram. For more details on our treating of the final-state interaction see sect. 4.2.

In a next step, total cross-sections for the reaction $pp \to pp\pi^0$ were extracted from the data by summing up the events for $\mathrm{m}_x \geq 0.13\,\mathrm{GeV}/c^2$ (see fig. 5). By making minute corrections for falsely interpreted $pp \to pn\pi^+$ events of order 3% from Monte Carlo considerations, one finds the number of $pp\pi^0$ events as given in column 3 of table 1. Column 4 lists the acceptances as derived from our Monte Carlo simulations. The main deviation from complete acceptance (acc $\equiv$ 1) results from geometrical properties as, *e.g.*, the central hole in the inner start detector (mainly for the low-energy measurements) and the missing ring component (see sect. 2.1) for the measurement at $T = 298.1\,\mathrm{MeV}$. Nevertheless, in all cases acceptance values of order 50% or higher were found. The error in acc was estimated by varying in the Monte Carlo code such values as the diameter of the central hole of the start detector (by some 10%) or the beam energy (by 0.2 MeV). An overall error of $\Delta\mathrm{acc} = 3.5\%$ was found. The integrated luminosities, as given in column 5 of table 1 were derived from a comparison with the results obtained for pp elastic scattering in the angular range 32°–55°, a range that was covered by the barrel alone. For the measurement at $T = 293.5\,\mathrm{MeV}$, where the ring was available as well, the quoted value not only is corroborated by the results found for the extended range 18°–70°, but also from a comparison with results for $pp \to d\pi^+$. For this reaction a total cross-section of $\sigma = 42 \pm 5\,\mu\mathrm{b}$ was found in very good agreement with an interpolated value of 44 μb deduced from [33]. For the $pp \to pn\pi^+$ reaction at $T = 298.1$ MeV we determined a cross-section of $\sigma_{pn\pi^+} = 3.5 \pm 0.4\,\mu\mathrm{b}$ which agrees nicely with the interpolated value of $3.1 \pm 0.4\,\mu\mathrm{b}$ extracted from [7,8].

Total cross-sections for the reaction $pp \to pp\pi^0$ are given in the last column of table 1 together with their statistical and systematical errors. The latter are composed of 5% from the pp cross-section, 3.5% from the acceptance correction, 1.5% from the uncertainty in misinterpreted background events and 2% in the luminosity determination.

4.2 Dalitz plots and energy distribution

As mentioned before, a crucial point in the determination of the total cross-section is the extrapolation of the measured data into the full region allowed by phase space. A thorough understanding of the detector response is essential, as is the knowledge of any deviation in the original (physical) data from those given by simple phase space, *i.e.*, s-wave–distributed events. A convenient way to compare in a comprehensive manner experimental and simulated data from a 3-particle reaction is to set up a Dalitz plot, which quite instructively allows the extraction of the underlying physics from the event distribution. Purely phase-space–distributed events will result in a uniformly covered Dalitz plot, deviations from such a distribution will induce some modulations. The Dalitz plot, as found from the present (kinematically fitted) data at $T = 293.5\,\mathrm{MeV}$, is shown in fig. 7 and compared to the result of our Monte Carlo simulation (top panel left and right, respectively). As a consequence of the strong final-state interaction in the pp system a systematic enhancement in the top left corner is observed in the data. The

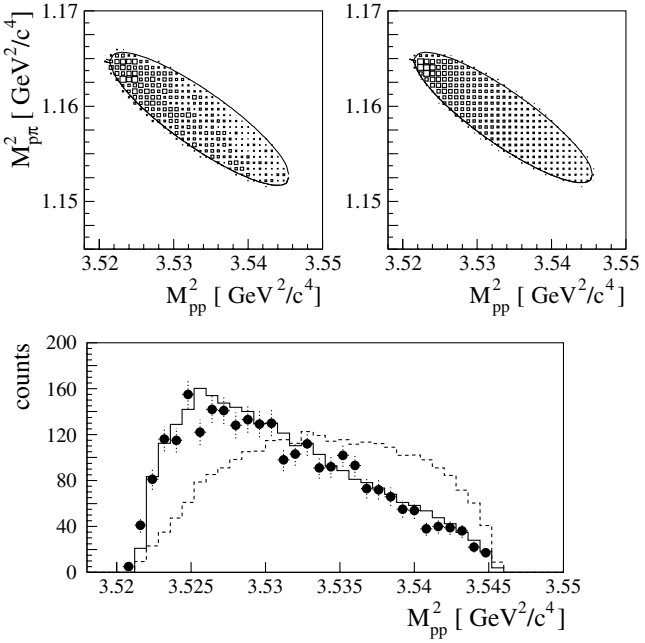

Fig. 7. Top: Dalitz plots of experimental (left) and simulated (right) data with kinematical limits given by the solid lines. The enhancement due to FSI is seen in the upper left corner of the event distribution. Bottom: projection of the Dalitz plots onto the M^2_{pp}-axis. Experimental data are given by solid dots with statistical error bars, the solid histogram shows the simulated distribution including FSI effects. The dashed histogram represents the simulated distribution for pure phase space.

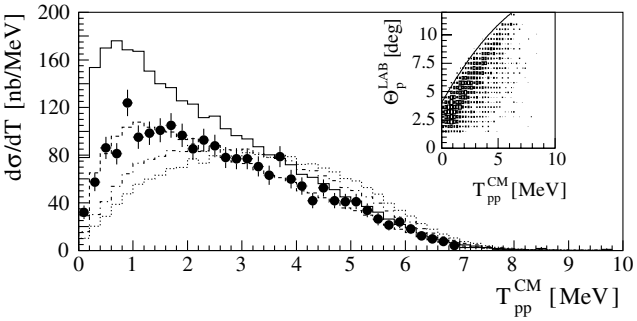

Fig. 8. Proton energy distribution $T^{\rm CM}_{pp}$ in the 2-proton CM system (solid dots with statistical error bars) in comparison with the Monte Carlo simulation including FSI with standard parameters (dashed histogram). The extrapolation to full acceptance is shown by the solid histogram. The pure phase space distribution is given by the dotted histogram, a simulation with FSI and a scattering length $a_0 = -1.5$ fm by the dash-dotted histogram. The insert shows $\Theta_p^{\rm LAB}$, the smaller of the two proton angles, *vs.* $T^{\rm CM}_{pp}$ (see text). The solid line denotes the upper boundary in $\Theta_p^{\rm LAB}$ as deduced from our MC simulation, the lower one coincides with the x-axis showing clearly the limit in our acceptance slightly below 2°.

simulated distribution was obtained by incorporating the FSI formalism as developed in [34,35] and later refined by Morton *et al.* [36]. In short, one calculates additional weight factors $w_{\rm fsi}$ which are multiplied with the event weight $w_{\rm e}$ given by the CERNLIB subroutine GENBOD (see also sect. 3.3). These factors are given as

$$w_{\rm fsi} = C^2 \cdot \left[C^4 \cdot T^{\rm CM}_{pp} + \frac{(\hbar c)^2}{m_p c^2} \times \left(\frac{m_p c^2}{2(\hbar c)^2} r_0 \cdot T^{\rm CM}_{pp} - \frac{1}{a_0} - \sqrt{2}\frac{\alpha m_p c^2}{\hbar c} \cdot h(\gamma_p) \right)^2 \right]^{-1}, \quad (2)$$

where $T^{\rm CM}_{pp}$ denotes the pp center-of-mass kinetic energy $T^{\rm CM}_{pp} = M_{pp} - 2m_p$ and C^2 the Coulomb penetration factor

$$C^2 = \frac{2\pi \cdot \gamma_p}{e^{2\pi\gamma_p} - 1} \quad (3)$$

with $\gamma_p = \frac{\alpha \cdot \mu_{pp} \cdot c}{p_{pp}}$. Here, α is the fine-structure constant, $p_{pp} = \sqrt{2\mu_{pp} T^{\rm CM}_{pp}}$ and μ_{pp} is the reduced mass of the pp system. The term with $h(\gamma_p) = \gamma_p^2 \cdot \sum_n \frac{1}{n(n^2+\gamma_p^2)} - 0.5772 - \ln\gamma_p$ contributes only little and is often omitted. From the literature we took the standard values $a_0 = -7.83$ fm and $r_0 = 2.8$ fm [37] as input parameters for the scattering length and effective range, respectively, for the two protons in the $^1S_0$-state. The smooth rise in yield, which readily is seen in the simulated data, is partially obscured in the experimental data due to the limited statistical accuracy. However, when inspecting the projection of the 2-dimensional Dalitz plot distribution onto the x-axis it is obvious that only through inclusion of FSI effects the simulated data follow the experimental ones (fig. 7, bottom), whereas a simulation based on purely phase-space–distributed events fails over the whole range.

The proton energy distribution $T^{\rm CM}_{pp}$ at 293.5 MeV in the center-of-mass system is shown in fig. 8. That close to threshold proton energies only range up to roughly 7 MeV with a very distinct maximum near 1 MeV. The FSI-based simulation given by the dashed histogram reproduces the data very well, whereas a simple phase space distribution (given by the dotted histogram and normalized to the experimental yield) fails completely. Also shown is the result of a simulation where final-state interaction effects have been included but with a much reduced scattering length of $a_0 = -1.5$ fm, as was suggested in [4] (fig. 8, dash-dotted histogram). When normalizing this distribution to our experimental data as was done in fig. 8, very poor agreement is observed. If, on the other hand, one normalizes only to the upper part beyond $T^{\rm CM}_{pp} = 3.0$ MeV, the maximum around 1.0 MeV is totally missed and we cannot see how a proper extrapolation can be achieved. From the insert showing in a two-dimensional plot $\Theta_p^{\rm LAB}$, the smaller of the two proton angles, *versus* $T^{\rm CM}_{pp}$, it can be seen that the maximum yield found near $T^{\rm CM}_{pp} = 1$ MeV is connected with one of the two protons emerging towards Θ values well below 5°, a range that is almost completely without detector coverage in each of the two internal target experiments. In view of this observation we argue that a description of the data and hence an extrapolation towards full acceptance can only be performed correctly by using the standard values $a_0 = -7.83$ fm and $r_0 = 2.8$ fm

as scattering length and effective range, respectively. The result is given by the solid histogram in fig. 8.

One important remark should be added. In the work of Flammang *et al.* on the $pp \to pn\pi^+$ reaction it was argued that the acceptance calculation and thus the extraction of a total cross-section is insensitive to the presence, absence or details of the FSI model [8], since the additional weight factors used for the extrapolation cancel out. This statement is true to some extent and has been checked in the present analysis; the extrapolation to full acceptance, as given in fig. 8 by the solid line, could also be obtained from our *experimental* points by neglecting in the Monte Carlo simulation any FSI effects and assuming purely phase-space–distributed events. The agreement between experimental and simulated data in that case, however, would have been of that quality shown in fig. 8 by the dotted line. Instead, and we like to stress this as a crucial point, our initial distribution, although modified by the detector acceptance, not only showed the enhancement due to FSI, but this distribution was also well reproduced by our Monte Carlo simulation, which we had based on i) our knowledge of detector performance and acceptance and ii) the use of standard FSI parameters for scattering length and effective range. If we had started from a distribution with (almost) no enhancement, nothing would have been gained from an extrapolation where one tries to adjust the w_{fsi} weights alone.

4.3 Angular distribution

Acceptance corrected angular distributions for the pion– and relative-two-proton–momentum vectors are shown in fig. 9 for the measurement at $T = 293.5\,\mathrm{MeV}$. The solid lines are the result of fits in terms of Legendre polynomials P_l to the experimental data $W(\cos\Theta) \propto 1 + \sum_l a_l \cdot P_l(\cos\Theta)$ up to $l = 2$. Only very small a_2-coefficients were found as expected that close to threshold, namely $a_2 = +0.05 \pm 0.10$ for the top and $a_2 = +0.08 \pm 0.11$ for the bottom distribution. Similar results were obtained at the other two bombarding energies. The observed symmetry around $\cos\Theta = 0$ (or the vanishing of the P_1-term), which stems from the entrance channel consisting of two identical particles, was not used as a constraint in the fit; instead, we consider it as a valuable check on the quality of our acceptance corrections.

The angular distribution obtained for the $pp \to pn\pi^+$ reaction at $T = 298.1\,\mathrm{MeV}$ corresponding to $\eta = 0.19$ was found to be consistent with isotropy which is in agreement with the published data [8]. Sizeable anisotropies were found for the angular distribution of the 2-particle reaction $pp \to d\pi^+$ yielding an a_2-coefficient of order $+0.2$ and larger with, however, an error of comparable size. This is a consequence of the significant acceptance corrections which had to be performed to account for those pions which had decayed before reaching the detector, as well as those which were too low in momentum as being able to reach the second layer of the endcap (see also sect. 3.3).

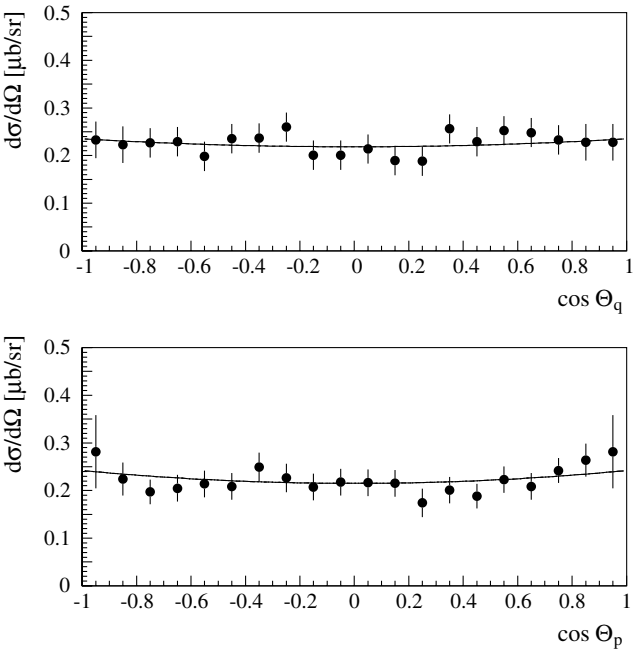

Fig. 9. Acceptance-corrected angular distributions in $\cos\Theta_q$ (direction of pion momentum) and $\cos\Theta_p$ (direction of relative two-proton momentum) in the CM system as obtained at $T = 293.5\,\mathrm{MeV}$. The solid lines are the result of Legendre polynomial fits up to $l = 2$.

5 Discussion

The total cross-sections listed in table 1 are compared to results found in the literature [1–3,5,6] in fig. 10. In the range $\eta = 0.2$–$1.0\,\sigma$ rises over two orders of magnitude up to values close to 100 μb. The present data exceed the ones from IUCF [1] and CELSIUS [3] by roughly 50%. We connect this discrepancy with the one basic difference in experimental set-up, namely theirs being an internal-, ours, however, an external-target experiment. The most critical step in extracting an absolute cross-section lies in the acceptance correction, which depends on the knowledge of i) geometrical coverage of the available phase space, ii) angular-distribution effects, and iii) deviations from s-wave–distributed events due to final-state effects. Since, most probably, the geometrical coverage is well accounted for in all three cases, and angular-distribution effects are negligible, we believe an underestimate of the strong FSI effects to be responsible for the large discrepancy. Our reasoning is as follows: The lower the energy above threshold, the more important the relative weight of FSI becomes, and, simultaneously, the more yield gets compressed into the very small angle region. If, on the other hand, the minimum angle is only near 4°, as is the case in the internal-target experiments at IUCF [1] or CELSIUS [3], more and more yield is missed. To extrapolate into the uncovered region requires a very profound knowledge of the original distribution, and most often some model dependence will enter the extrapolation procedure. As was mentioned before, the data given in [1] were corrected by using non-standard FSI parameters (scattering length

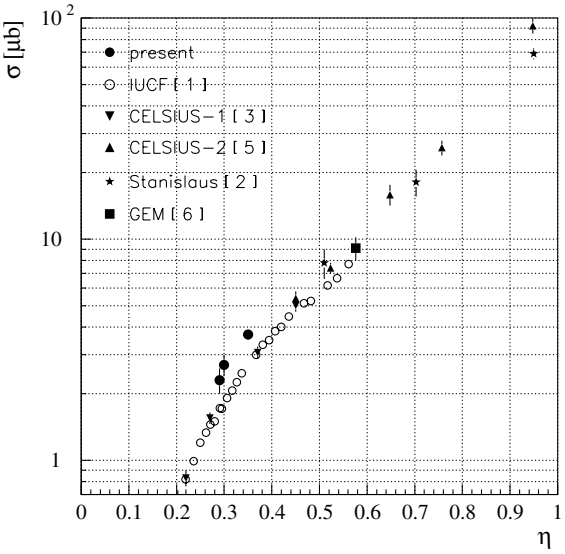

Fig. 10. Summary of cross-section data as known today for $pp \to pp\pi^0$ up to $\eta = 1.0$. The present data given by solid dots clearly are higher than the earlier ones from IUCF (open circles, [1]) and CELSIUS (solid downward triangles, [3]).

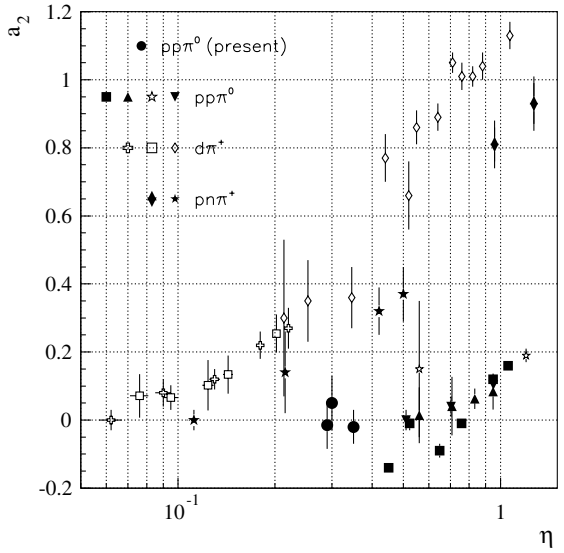

Fig. 11. Comparison of experimental a_2-coefficients as obtained from Legendre polynomial fits to π angular distributions in the near-threshold region. $pp \to d\pi^+$ data are given by open symbols, the ones for $pp \to pn\pi^+$ by solid asterisks and diamonds. Solid dots, squares and triangles as well as open asterisks are used to denote the data for $pp \to pp\pi^0$ (see text).

$a_0 = -1.5\,\mathrm{fm}$), an approach which completely failed to reproduce our data. The low-energy CELSIUS-data [3] were obtained by detecting the two decay photons instead of the two emerging protons, a method with an acceptance which is only weakly dependent on excess energy and is free of any threshold effects, but suffers from the very small geometric coverage of only 5%. A rather elaborate acceptance correction has been developed for the high-energy CELSIUS data [5] where FSI and angular-distribution effects were considered. As can be seen from fig. 10, these data exceed the previous IUCF data [1] as well, although by a smaller margin of some 15%.

A summary of Legendre polynomial expansion coefficients a_2 found in the literature for the pion-producing reactions in the near-threshold region is shown in fig. 11 as a function of η. Three bands of data are discernible. The fastest rise with η is observed for the $pp \to d\pi^+$ reaction (given by open symbols, refs. [10,11,38]), where deviations from $a_2 = 0$ are already found below $\eta = 0.1$. The positive a_2-coefficients are an indication for strong p-wave contributions. Much less information is available for the other π^+-producing reaction measured at IUCF and TRIUMF and plotted as asterisks [8] and diamonds [39], respectively. Yet, a comparable behaviour of a fast rise can be observed as well, which, however, only starts somewhat later near $\eta = 0.2$. For both these reactions with an isoscalar two-nucleon pair in the exit channel the Sp partial wave, which is not Pauli forbidden, contributes almost from threshold. A totally different pattern is observed in case of the $pp \to pp\pi^0$ reaction. Near-isotropy is found for almost the whole η range shown in fig. 11 with a_2 staggering between -0.2 and $+0.2$. It is not clear whether d-wave contributions which induce negative a_2-coefficients might be present that close to threshold. A unique trend (toward positive values) is only observed for $\eta > 0.9$.

To get a more quantitative estimate on the amount of p-wave contributions to the $pp\pi^0$ reaction at $\eta = 0.3$ we used the fact that close to threshold the dynamics for pion production as given by the matrix element is almost energy independent. Instead, the rapid rise in cross section is governed by kinematical effects, since phase space as well as the radial wave functions of the participating particles change drastically. In a non-relativistic treatment the available phase space volume scales as $q \cdot p$. The wave functions can be approximated by their asymptotic form which is valid for small arguments, and from this one obtains a factor $q^{l_q} \cdot p^{l_p}$ with l_q (l_p) denoting the angular momentum of the pion (the NN pair), respectively. Hence, each of these additional terms has a particular momentum dependence as, *e.g.*, $\sigma_{Ps} \propto q \cdot p^3$ and $\sigma_{Pp} \propto q^3 \cdot p^3$ [19]. To account for these higher-order terms, we introduced into our Monte Carlo code additional weight factors $w_{Ps} = C_{Ps}^2 \cdot qp^3$ and $w_{Pp} = C_{Pp}^2 \cdot p^3 q^3$ with adjustable fit parameters C_{Ps}^2 and C_{Pp}^2, which were added to the dominant weight $w_\mathrm{e} \cdot w_\mathrm{fsi}$ discussed in sect. 4.2. Due to the limited statistical accuracy in our data we did not attempt a combined fit where the Ps and Pp fractions were varied simultaneously. Instead, we fitted our experimental q- and p-momentum distributions by a Monte-Carlo–generated sum of either $Ss + Ps$ or $Ss + Pp$ terms. In view of the good overall acceptance of our detector with only a small central hole of slightly less than 2° any acceptance dependence of the weight factors, however, was neglected. The resulting χ^2 values as obtained for various fractions f are shown in table 2 where f is given through $\sigma_{Ps(p)} = f \cdot \sigma$ and $\sigma_{Ss} = (1 - f) \cdot \sigma$. The best fit with a reduced $\chi^2/n = 1.24$ with $n = 65$ degrees of freedom is found for pure s-wave behaviour. Up to 10% of a Pp contribution is allowed by the fit, Ps

Table 2. Reduced χ^2 values derived from fitting Monte-Carlo–generated momentum distributions to our experimental data by varying the amount of Ps or Pp contributions (see text).

$L_p l_q$	Ps				Pp			
f	0	0.05	0.10	0.20	0	0.05	0.10	0.20
χ^2/n	1.24	1.41	1.93	4.15	1.24	1.26	1.36	1.90

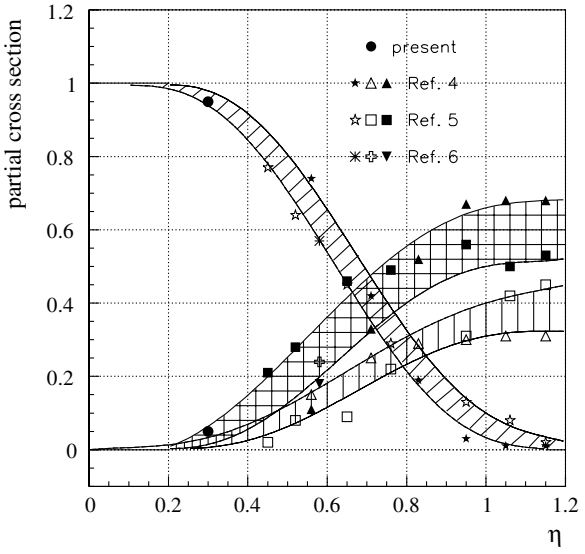

Fig. 12. Summary of partial cross-sections σ_{Ll}/σ *vs.* η. The present results are given by the full circles. Solid symbols (squares and triangles) which form the cross-hatched band denote σ_{Pp}, open squares and triangles in the vertically hatched band represent σ_{Ps}. σ_{Ss} is given by stars and asterisks (diagonally hatched band).

contributions are even weaker. As a result we assign to the Ss-strength for the $pp\pi^0$ reaction at $\eta = 0.3$ a fraction $(1 - f) = 0.95 \pm 0.05$, leaving only a minute contribution of 0.05 ± 0.05 for Pp and Ps-waves.

In fig. 12 we show the presently deduced partial cross-sections as a function of η together with data found in the literature [4–6]. Although some discrepancies in the data exist, which we attribute to the different methods applied, the general trend seems to be pretty much established. Up to $\eta = 0.7$ Ss given by the diagonally hatched band is the strongest, but gets almost negligible above $\eta = 0.9$. At the same time the Pp strength (cross-hatched band) starts to dominate, but saturates near 0.6. The Ps strength (vertically hatched band) seems to be present already below $\eta = 0.4$ and exceeds Ss near $\eta = 0.8$. In the crossover region the discrepancies are the largest, which, most probably, is due to the different methods used. The studies carried out at CELSIUS [5] and COSY-GEM [6] were also performed with unpolarized beam and target; from these experiments sizeable Pp strength was reported well below $\eta = 0.6$. A much higher sensitivity can be expected when measuring polarization observables as was recently done at IUCF [4]. In that study, σ_{Ps} was found to be larger than σ_{Pp} near $\eta = 0.56$.

Up to $\eta = 0.7$ the Ss partial wave dominates the $pp\pi^0$ reaction. As was pointed out in [17], the cross-section in this region could only be reproduced satisfactorily when adding an extra heavy-meson exchange (HME) contribution with a "free" strength parameter to the coherent sum of direct and rescattering terms, both of which make up roughly 60% of the measured yield. Yet, at energies above $\eta = 1$ where even higher partial waves with $l \geq 2$ start to contribute significantly and where Δ-isobar contributions have to be considered, the predictions underestimate the data more and more. In view of the present findings of a much larger cross-section also at low η values which would require an even larger strength parameter for HME contributions, it might be conceivable that something more essential is missing in the theoretical description of the near-threshold $pp\pi^0$ reaction. It seems to be worth mentioning that poor agreement is also found in recent calculations of polarization observables [40].

6 Summary

The $pp \to pp\pi^0$ reaction has been investigated in a kinematically complete experiment by detecting the two protons in the large acceptance spectrometer COSY-TOF set up on an external beam line of the proton synchrotron COSY. The calibration of the detector and the luminosity determination was carried out by analysing the pp elastic-scattering reaction recorded simultaneously. Extensive Monte Carlo simulations were carried out in order to determine the overall acceptance with high precision. Results derived for the concurring reactions $pp \to d\pi^+$ and $pp \to pn\pi^+$ are in very good agreement with data from the literature. Total cross-sections for the reaction $pp \to pp\pi^0$ were obtained at bombarding energies of 292.2, 293.5 and 298.1 MeV, which exceed previous measurements by roughly 50%. Invariant mass and energy distributions are governed by strong final-state effects. The importance of detecting protons well below 4° to the beam axis is stressed. The angular distributions for the pion– and relative-two-proton–momentum vectors were measured for η values as low as $\eta = 0.3$ and were found to be nearly isotropic as expected that close to threshold. From an analysis of the corresponding momentum distributions the combined fraction for Ps and Pp partial cross-sections was estimated to be $5 \pm 5\%$.

The help of the COSY crew in delivering a low-emittance proton beam is gratefully acknowledged. The data are based in part on the analysis work performed by B. Jakob [27]. We like to thank R. Klein and M. Würschig-Pörsel for their continued assistance in solving technical problems. Helpful discussions with C. Hanhart are very much appreciated. Financial support was granted by the FFE fund of the Forschungszentrum Jülich and by the German BMBF.

References

1. H.O. Meyer *et al.*, Nucl. Phys. A **539**, 633 (1992).
2. S. Stanislaus *et al.*, Phys. Rev. C **44**, 2287 (1991).
3. A. Bondar *et al.*, Phys. Lett. B **356**, 8 (1995).
4. H.O. Meyer *et al.*, Phys. Rev. C **63**, 064002 (2001).
5. R. Bilger *et al.*, Nucl. Phys. A **693**, 633 (2001).
6. GEM Collaboration (M. Betigeri *et al.*), Phys. Rev. C **65**, 064001 (2002).
7. J.G. Hardie *et al.*, Phys. Rev. C **56**, 20 (1997).
8. R.W. Flammang *et al.*, Phys. Rev. C **58**, 916 (1998).
9. W.W. Daehnick *et al.*, Phys. Rev. C **65**, 024003 (2002).
10. M. Drochner *et al.*, Phys. Rev. Lett. **77**, 454 (1996).
11. P. Heimberg *et al.*, Phys. Rev. Lett. **77**, 1012 (1996).
12. T.-S. Lee, D.O. Riska, Phys. Rev. Lett. **70**, 2237 (1993).
13. B.-Y. Park *et al.*, Phys. Rev. C **53**, 1519 (1996).
14. T.D. Cohen *et al.*, Phys. Rev. C **53**, 2661 (1996).
15. U. Van Kolck *et al.*, Phys. Lett. B **388**, 679 (1996).
16. M.T. Peña *et al.*, Phys. Rev. C **60**, 045201 (1999).
17. C. Hanhart *et al.*, Phys. Lett. B **444**, 25 (1998).
18. C. Hanhart *et al.*, Phys. Rev. C **61**, 064008 (2000).
19. A.H. Rosenfeld, Phys. Rev. **96**, 130 (1954).
20. The COSY-TOF Collaboration, Phys. Lett. B **429**, 195 (1998).
21. M. Dahmen *et al.*, Nucl. Instrum. Methods Phys. Res. A **348**, 97 (1994).
22. A. Böhm *et al.*, Nucl. Instrum. Methods Phys. Res. A **443**, 238 (2000).
23. A. Hassan *et al.*, Nucl. Instrum. Methods Phys. Res. A **425**, 403 (1999).
24. P. Michel *et al.*, Nucl. Instrum. Methods Phys. Res. A **408**, 453 (1998).
25. L. Karsch *et al.*, Nucl. Instrum. Methods Phys. Res. A **460**, 362 (2001).
26. R.A. Arndt *et al.*, Phys. Rev. C **62**, 034005 (2000); see also: *Scattering Analysis Interactive Dial-in*, URL: `http://said.phys.vt.edu`
27. B. Jakob, PhD Thesis, Technische Universität Dresden (2001).
28. S. Brand, PhD Thesis, Ruhr-Universität Bochum (1995).
29. U. Zielinsky, PhD Thesis, Ruhr-Universität Bochum (1999).
30. GENBOD, CERN Program Library Long Write-up W515 (1993).
31. P. Cloth, in *MC93, International Conference on MC Simulations in High Energy and Nuclear Physics*, edited by P. Dragovitch, S.L. Linn, M. Burbank (World Scientific, Singapore, 1994) p. 56.
32. H.W. Bertini, Phys. Rev. **188**, 1711 (1969).
33. M. Drochner *et al.*, Nucl. Phys. A **643**, 55 (1998).
34. K.M. Watson, Phys. Rev. **88**, 1163 (1952).
35. A.B. Migdal, Sov. Phys. JETP **1**, 2 (1955).
36. B.J. Morton *et al.*, Phys. Rev. **169**, 825 (1968).
37. H.P. Noyes, Annu. Rev. Nucl. Sci. **22**, 465 (1972).
38. B.G. Ritchie *et al.*, Phys. Rev. Lett. **66**, 568 (1991).
39. R.G. Pleydon *et al.*, Phys. Rev. C **59**, 3208 (1999).
40. C. Hanhart, in *MESON2002*, edited by L. Jarczyk, A. Magiera, C. Guaraldo, H. Machner (World Scientific, Singapore, 2003) p. 363, nucl-th/0207015.